Direct Observation of the Primary and Secondary C−Br Bond Cleavages from the 1,2-Dibromopropane Photodissociation at 234 and 265 nm Using the Velocity Map Ion Imaging Technique†

Kyoung-Seok Lee,‡ Ki Young Yeon, Kyung-Hoon Jung, and Sang Kyu Kim*

Department of Chemistry and School of Molecular Science (BK21), KAIST, Daejeon 305-701, Republic of Korea

Received: March 15, 2008; Revised Manuscript Received: June 26, 2008

Photodissociation dynamics of 1,2-dibromopropane has been investigated at 234 and 265 nm by using the velocity map ion imaging method. At both pump energies, a single Gaussian-shaped speed distribution is observed for the Br*($^2P_{1/2}$) fragment, whereas at least three velocity components are found to be existent for the Br($^2P_{3/2}$) product. The secondary C−Br bond cleavage of the bromopropyl radical which is energized from the ultrafast primary C−Br bond rupture should be responsible for the multicomponent translational energy distribution at the low kinetic energy region of Br($^2P_{3/2}$). The recoil anisotropy parameter (β) of the fragment from the primary C−Br bond dissociation is measured to be 0.53 (0.49) and 1.26 (1.73) for Br($^2P_{3/2}$) and Br*($^2P_{1/2}$), respectively, at 234 (265) nm. The β value of Br($^2P_{3/2}$) from the secondary C−Br bond dissociation event at 265 nm is found to be 0.87, reflecting the fact that the corresponding Br($^2P_{3/2}$) fragment carried the initial vector component of the bromopropyl radical produced from the primary bond dissociation event. Density functional theory has been used to calculate energetics involved both in the primary and in the secondary C−Br bond dissociation dynamics.

Introduction

Photodissociation dynamics of alkyl halides have been both extensively and intensively studied for recent decades. The diffuse absorption feature at UV reflects the repulsive nature of the potential energy surface along the carbon−halogen bond elongation axis.[1−23] Because of the strong spin−orbit coupling of the halogen atom, however, the dissociation dynamics involves nonadiabatic crossing from which the well-defined spin−orbit states of the halogen atomic fragment are generated at the asymptotic limit. Because of these interesting features, alkyl halides have been spotlighted as the prototypical system of the direct dissociation dynamics study not only for the detailed nuclear rearrangement during the fragmentation but also for exploring the Landau−Zener-type nonadiabatic coupling dynamics.[11−20,22,24,25]

In this work, we have focused on the dynamics of 1,2-dibromopropane in which two almost equivalent C−Br bonds are subject to dissociation upon the single UV photon excitation. The dissociation dynamics of two equivalent bonds in the same molecule has received special attention because of the issue of the concertedness of two fragmentation events.[26−30] For instance, two equivalent C−C bonds of acetone, excited at 157 nm, are found to break apart in a stepwise manner when those events are monitored in the femtosecond real time scale.[31] Such a real-time observation of the bond-breaking and bond-formation events gives a direct clue for resolving the issue of the concertedness because the nuclear arrangement in real time is used for the judgment of the concertedness.[31−33] For dynamics details, however, the measurement of speed and angular distribution of fragments is essential especially for the elucidation of the potential energy surfaces on the exit region, where the energy disposal to fragments is determined. Nowadays, the velocity map ion imaging technique is very well established, and it is very convenient to extract speed and angular distributions of fragments at the same time.[33−38] We have measured the speed and angular distributions of both ground and spin−orbit excited states of Br from the dissociation of 1,2-dibromopropane by using the velocity map ion imaging method. Interestingly, both primary and secondary dissociation events are reflected in the product ion images, giving a detailed picture of the dynamics in terms of the energy disposal and energetics involved in the dissociation pathway taking place in a stepwise manner. It is found that the velocity map ion imaging technique allows the direct observation of two dissociation events in a spatially separated way. Density functional theory (DFT) is employed to calculate the energetics involved in the overall dissociation process.[39]

Experimental Methods

The velocity map ion imaging setup has been described elsewhere in detail.[32−36] The 2% gas mixture of 1,2-dibromopropane (Aldrich, 97%) seeded in the He carrier gas was injected into a source chamber through a nozzle orifice (General Valve 9 series) at a repetition rate of 10 Hz. The supersonic jet was then skimmed through a 1 mm diameter skimmer prior to be intersected by the laser pulse at a right angle. The background pressures of the source and ionization chambers were maintained at 10^{-6} and 10^{-8} Torr, respectively, when the nozzle was on. The third harmonic output of a Nd:YAG laser (Spectra-Physics, GCR-170) was used to pump a dye laser (Lumonics, HD-500) to generate the tunable laser pulse. The visible dye laser output was then frequency doubled via a BBO crystal to give the UV laser pulse output. The UV laser pulse at 233.96 and 264.85

† Part of the "Stephen R. Leone Festschrift".

* Author to whom correspondence should be addressed. Fax: (82)-42-869-2810. E-mail: sangkyukim@kaist.ac.kr.

‡ Current address: Korea Research Institute of Standards and Science, Daejeon 305-600, Republic of Korea.

10.1021/jp8022666 CCC: $40.75

Published on Web 07/30/2008

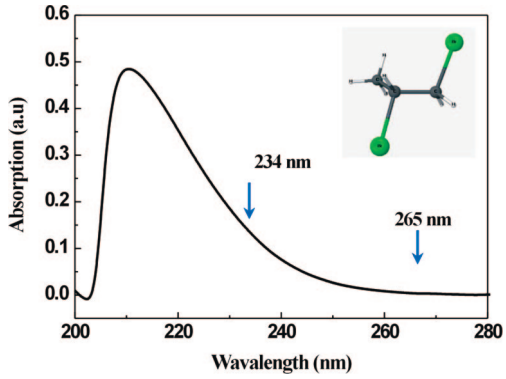

Figure 1. UV absorption spectrum of 1,2-dibromopropane in *n*-hexane solvent. The wavelengths employed in this work are designated by the arrows.

nm was used for the (2 + 1) ionization of Br*($^2P_{1/2}$) via the 6p $^2S_{1/2}$ or 5p $^2P_{1/2}$ states, respectively, whereas the transitions at 233.79 and 264.75 nm were used by the (2 + 1) ionization of Br($^2P_{3/2}$) via the 6p $^4P_{5/2}$ and 5p $^4D_{7/2}$ states, respectively. The UV laser pulse was focused onto the molecular beam for both pump and probe purposes. The polarization of the laser pulse was parallel to the position-sensitive detector and perpendicular to the time-of-flight axis. The resultant Br ions were repelled, accelerated, drifted along the field free region, and detected by the microchannel-plates-equipped position-sensitive detector with a mass-gated electric pulse. An image intensifier (Stanford Computer Optic) coupled with a charge-coupled device camera (Photometric, CH250) was used to digitize the ion images. The voltages applied to the ion optics were carefully adjusted for the velocity mapping condition. The images were averaged over 10 000 laser shots and stored in a personal computer. Raw ion images were reconstructed by using the basis-set expansion (BASEX) algorithm.[40]

Results and Discussion

The absorption spectrum of 1,2-dibromopropane shows the broad featureless band starting from near 280 nm with the maximum intensity at ~210 nm, Figure 1. Three different optical transitions of which the transition dipole moments are either parallel or perpendicular to the C−Br bond are responsible for such a broad absorption band. Even though the contribution of each electronic transition strongly depends on the excitation wavelength, all of the electronic transitions contain the σ^* character along the C−Br bond inducing the ultrafast C−Br bond rupture to give the ground (Br) and excited (Br*) states of the bromine atom at the asymptotic limit. Because the main focus of this work is on the dynamics of the primary and secondary C−Br bond dissociations, relative oscillator strengths of three electronic transitions and associated nonadiabatic coupling dynamics are not discussed here, although such information could be extracted from the careful measurement of the relative product yields and associated anisotropy parameters.[38]

Raw and reconstructed ion images of Br and Br* from 1,2-dibromopropane excited at 234 nm are shown in Figure 2. Whereas the Br* image shows an anisotropic sharp ring, the image due to Br is found to be less anisotropic and quite broadened. The difference of the Br and Br* images is more dramatic at the excitation energy of 265 nm. Similarly to the case of 234 nm, the Br* image consists of the single anisotropic ring of which the corresponding translational energy distribution is well-fitted by the single Gaussian-shaped function, Figures 3 and 4. However, the Br ion image taken at 265 nm shows the peanut-shaped image, indicating that the Br fragment has a broad translational distribution, and yet, its angular distribution is quite anisotropic. The Br translational energy distribution at 265 nm shows the distinct bimodal distribution, indicating that there are at least two different reaction pathways giving the Br fragment from the 1,2-dibromopropane at this pump energy. In order to resolve the different reaction pathways, the energetic involved in the following reactions need to be considered.

$$C_3H_6Br_2 + h\nu \rightarrow \bullet C_3H_6Br + Br(Br^*) \quad (1)$$

$$\bullet C_3H_6Br \rightarrow C_3H_6 + Br \quad (2)$$

The first reaction is the direct C−Br bond dissociation upon the nσ^* optical excitation. Because absorption bands of two C−Br bonds in 1,2-dibromopropane are expected to be only slightly different and not separable in our excitation scheme, the average value of two different C−Br bond energies is used for the calculation of energetics. The DFT calculation with the B3LYP method using the basis set of 6-311++G (3df, 3pd) was used for the evaluation of the bond energy for the primary bond dissociation, giving D_0'(C−Br) = 59.02 kcal/mol. After the ultrafast photoinduced C−Br bond rupture, the available energy corresponding to the difference between the photon and bond dissociation energies is partitioned into translational and internal energies of fragments. By taking the translational energy of fragments from the experimentally measured distribution, Table 1, the average internal energy of the nascent C_3H_6Br radical at 234 nm is estimated to be 39.5 and 30.3 kcal/mol for the Br and Br* channels, respectively. For the Br channel, only the Gaussian-shaped component found at the high-energy region is used for the calculation of the average translational energy. Although the optimized geometries of 1-bromopropyl and 2-bromopropyl radicals are quite different, Figure 5, the secondary C−Br bond dissociation energies of these radicals are calculated to be almost equal to give the average value of D_0''(C−Br) = 12.68 kcal/mol. It should be noted that the reaction threshold could be higher than the dissociation energy because of the presence of a reaction barrier. It is interesting to note that the 2-bromopropyl radical adopts the bridged shape at the minimum energy structure with the C−Br bond length of 3.02 Å which is much longer than that of 1-bromopropyl radical.

The secondary C−Br bond dissociation from the vibrationally hot C_3H_6Br radical then takes place in the ground electronic state. The C−Br bond dissociation of the bromopropyl radical most likely produces the propene molecule and Br through the molecular channel on which two neighboring unpaired orbitals of the transient diradical combine to form a stable chemical bond in propene. Therefore, unlike the radical channel on which the parent ground state smoothly correlates to the product states, a certain reaction barrier is expected to be present along the reaction coordinate for the C−Br bond cleavage of the C_3H_6Br radical. The translational energy distribution of the secondary Br product, the shape of which is dependent on the internal energy of the nascent C_3H_6Br radical, should be then convoluted with the Gaussian-shaped energy distribution of C_3H_6Br which is acquired from the primary bond dissociation event (vide infra). It should be noted that the translational energy partitioning is not expected to be large during the secondary dissociation because the energy randomization prior to bond breaking should lead to the more activation of the internal modes of fragments rather than the activation along the recoil direction. Even after the assumption of the Gaussian-shaped distribution for Br from

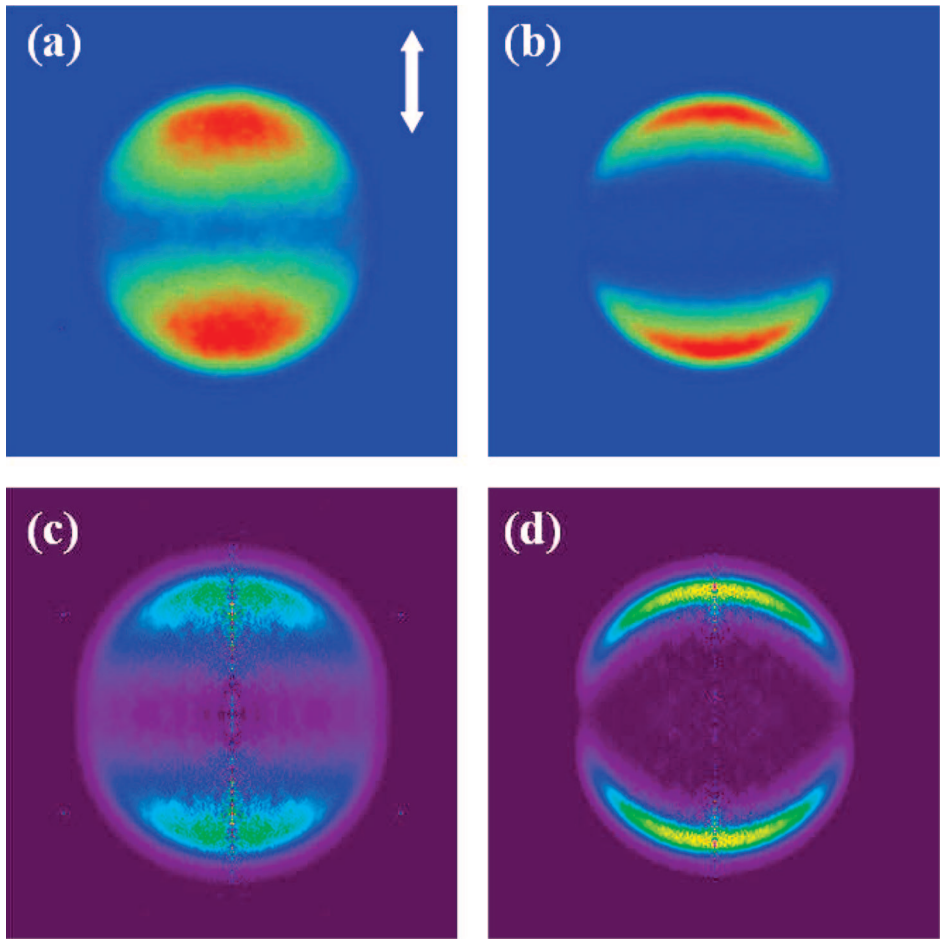

Figure 2. Raw images of (a) Br and (b) Br* in the photodissociation of 1,2-dibromopropane at 234 nm. Corresponding three-dimensional reconstructed images of Br and Br*, obtained by using the BASEX algorithm, are represented in (c) and (d), respectively. In all images, the linearly polarized pump lasers have the plane of polarization vertical to the time-of-flight axis, as shown by a vertical arrow.

all channels, the deconvolution of the secondary Br fragment out of the total distribution at 234 nm turns out to be not trivial, although three velocity components of Br seem to reproduce the experiment nicely, Figure 4.

The contribution from the secondary C−Br bond breakage to the Br image is more pronounced at 265 nm, Figure 4. This is partly due to the narrower energy distribution of primary products at the pump energy of 265 nm compared to that at 234 nm, as clearly observed in the Br* translational energy distributions at two pump wavelengths. The internal energy of C_3H_6Br radical at 265 nm is estimated to be 29.2 and 21.4 kcal/mol from the primary Br or Br* channels, respectively. Considering the fact that the C_3H_6Br radical with the higher internal energy will be responsible for Br of the higher kinetic energy from the secondary dissociation, a Gaussian-shaped component peaked at ~5 kcal/mol is ascribed to the secondary Br fragment from the C_3H_6Br radical generated by the primary C_3H_6Br + Br channel, whereas the small component peaked at ~2 kcal/mol may be due to Br from the C_3H_6Br radical produced by the primary C_3H_6Br + Br* channel. Actually, the spatial distribution in the Br image at 265 nm is quite interesting. Two spherical-shape split into up and down suggests that the secondary Br fragment may be isotropic, whereas the initial recoil velocity imparted to the C_3H_6Br radical is responsible for the underlying peanut-shaped vertical anisotropic distribution. Because the secondary dissociation rate is expected to be slow at the low internal energy of the C_3H_6Br radical generated at 265 nm, the isotropic distribution of the secondary Br fragment indicating that the dissociation time constant is larger than the rotational constant of ~1 ps is quite reasonable.

Further dynamic details for the secondary dissociation including the energy disposal and reaction rate involved in the present experiment are hardly extractable though because of the complicated nature of the Br ion image taken in this work. It should be noted that for the secondary Br fragment, the quantitative analysis of the translation energy directly from the ion image might be less meaningful because the secondary C−Br dissociation occurs on the fast recoiling C_3H_6Br radical from the primary C−Br bond dissociation. Namely, the velocity vector of the C_3H_6Br radical attained from the primary bond cleavage should always be added to the velocity vector of Br from the secondary dissociation. From the simple kinematics of the momentum conservation, the most probable translational energy of the C_3H_6Br radical calculated from that of the primary Br product is depicted as an arrow for each pump wavelength of 234 or 265 nm, Figure 4. It is interesting to note that the most probable translational energy of C_3H_6Br matches relatively well with the peak of the translational energy component due to the secondary Br fragment at 234 nm, Figure 4b. On the other hand, the peak of the secondary Br energy distribution deconvoluted from the Br distribution at 265 nm is found to be red-shifted with respect to the most probable translational energy of C_3H_6Br calculated from the peak position of the primary Br distribution, Figure 4d. This experimental observation suggests that, because of the smaller average internal energy of the nascent C_3H_6Br radical at 265 nm compared to that at 234 nm,

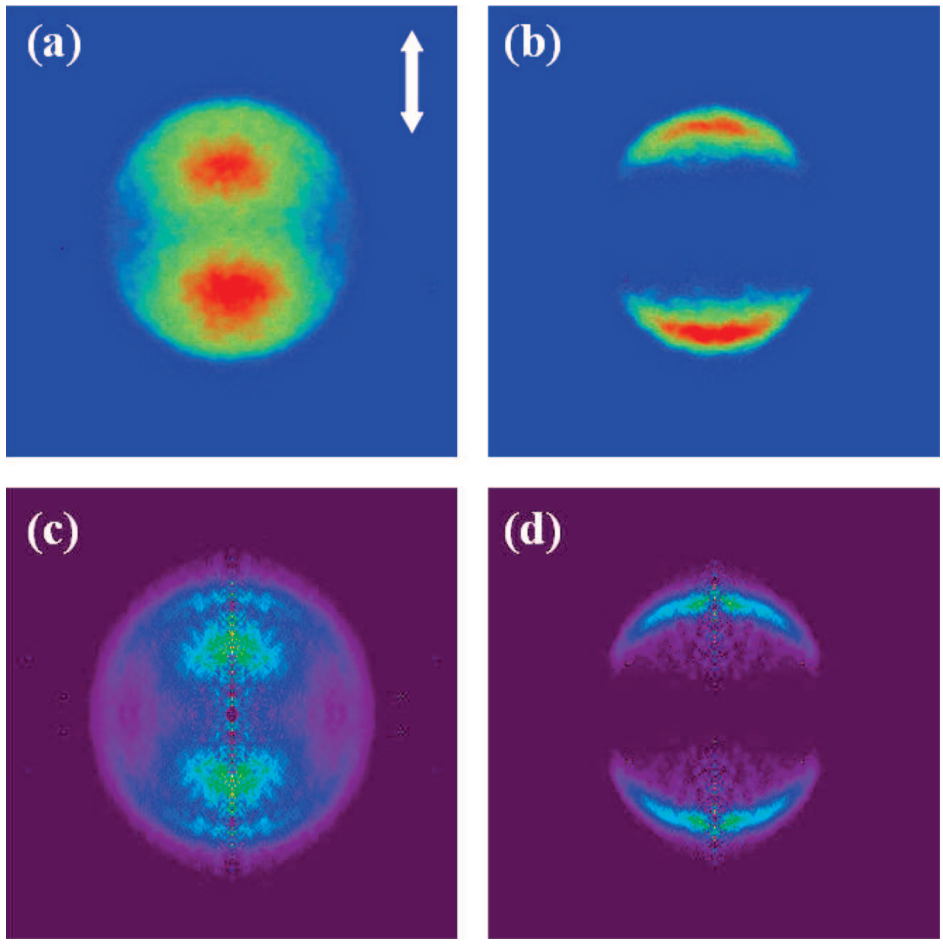

Figure 3. Raw images of (a) Br and (b) Br* in the photodissociation of 1,2-dibromopropane at 265 nm. Corresponding three-dimensional reconstructed images of Br and Br*, obtained by using the BASEX algorithm, are represented in (c) and (d), respectively.

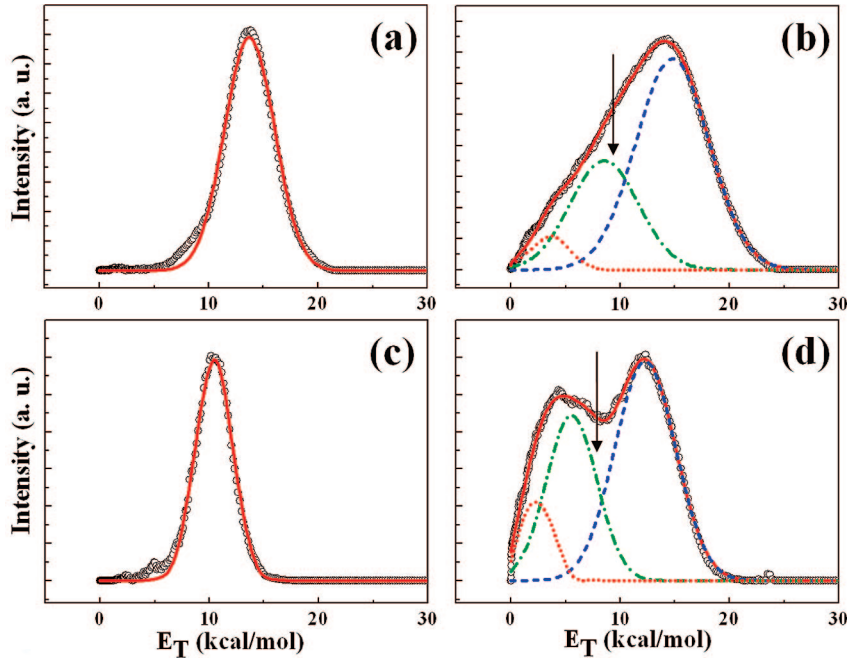

Figure 4. Translational energy distributions of Br fragments in the photodissociation of 1,2-dibromopropane, (a) Br* and (b) Br at 234 nm and (c) Br* and (d) Br at 265 nm. At both wavelengths, the experimental data (open circles) are well fitted by a single Gaussian function for Br*, whereas at least three Gaussian functions are required to reproduce the experimental data for Br. See the text for details. Arrows in (b) and (d) represent the most probable translational energies of the C_3H_6Br radical acquired from the primary dissociation at 234 and 265 nm, respectively.

the secondary dissociation occurs only partially for the C_3H_6Br radical at 265 nm, whereas it takes place more efficiently at 234 nm.

There are several other factors which need to be considered in the interpretation of the ion image of Br. First, it should be noted that Br from the secondary C−Br bond cleavage can be

TABLE 1: C−Br Bond Dissociation Energies of 1,2-Dibromopropane Calculated by DFT with the B3LYP Method by Using a 6-311++G(3df,3pd) basis set (kcal/mol)

	dissociation energy (kcal/mol)
1,2-dibromopropane → 1-bromopropyl radical + Br^{1st}	58.89
1,2-dibromopropane → 2-bromopropyl radical + Br^{1st}	59.14
1-bromopropyl radical → C_3H_6 (propene) + Br^{2nd}	12.81
2-bromopropyl radical → C_3H_6 (propene) + Br^{2nd}	12.55

seen in the image only when the secondary dissociation event occurs within the laser pulse width of 5 ns. In other words, the Br fragment coming from the reaction slower than the time duration of the laser pulse cannot be ionized. When considering the small energy difference between the intermediate radical and asymptotic fragments in the secondary dissociation event, however, the 5 ns may be long enough to cover most of fragments except those being generated near the reaction threshold. Another point is that the low velocity component of the C_3H_6Br radical would have a better chance to be seen in the Br ion image because the slower radical gains a higher internal energy from the primary bond breakage. This may explain the difference between the Br distributions at 234 and 265 nm in terms of the peak positions of the secondary Br energy distributions with respect to the most probable energies of the C_3H_6Br fragments, Figure 4. It should also be noted that the relative contributions of the primary and secondary Br in the total Br distribution result from many dynamic parameters such as the Br/Br* branching ratio and the energy partitioning in both primary and secondary dissociations. Therefore, the Br translation energy distribution is the result of many interesting dynamical aspects, although its analysis is not straightforward at the present time.

The recoil anisotropy parameter (β) of the fragment which is deduced exclusively from the primary C−Br bond dissociation is determined to be 0.53 (0.49) and 1.26 (1.73) for $Br(^2P_{3/2})$ and $Br^*(^2P_{1/2})$, respectively, at 234 (265) nm. Because the Br* product is diabatically correlated for the excited-state with the transition dipole moment parallel to the C−Br bond axis, anisotropy values close to the limiting value of 2 are observed at 265 nm. As mentioned earlier, relative oscillator strengths of three different electronic transitions and associated nonadiabatic couplings along the three repulsive potential energy surfaces are responsible for those anisotropy parameters determined for the primary C−Br bond cleavage. It is interesting to note that β of $Br(^2P_{3/2})$ deduced only from the secondary C−Br bond dissociation at 265 nm is found to be 0.87, indicating that the corresponding $Br(^2P_{3/2})$ fragment is carrying the initial vector component of the bromopropyl radical produced from the primary bond cleavage. The higher anisotropy value of the secondary Br compared to that of the primary Br suggests that only partial portion of the nascent C_3H_6Br fragment may undergo the secondary C−Br bond dissociation, which is consistent with the red shift of the translational energy distribution of the secondary Br at 265 nm in Figure 4d (vide supra).

Conclusions

In this work, it has been demonstrated that the primary and secondary bond dissociation events can be directly observed by using the velocity map ion imaging method. Two almost equivalent C−Br bonds of 1,2-dibromopropane are found to be cleaved in a stepwise manner at pump energies of 234 and 265 nm. The Br* ion image shows a single Gaussian-shaped translational energy distribution, whereas three different velocity components contribute to give the Br translational energy distribution. The secondary C−Br bond breakage of the internally hot C_3H_6Br radical should be responsible for the relatively low kinetic energy components of the total distribution. The secondary Br fragment is observed as the vector sum of itself and the photon-induced recoiling C_3H_6Br fragment from which the secondary dissociation occurs. The quantitative analysis of the image regarding the secondary C−Br bond cleavage turns out to be not straightforward because of the complicated nature of the Br ion image. However, the intriguing dynamical features in the 1,2-dibromopropane photodissociation are revealed in the ion image quite distinctly for each dissociation event. Especially, it is noteworthy that the spatial separation of the primary and secondary events occurring in the same molecule is observed for the first time in the two-dimensional ion image, promising that the direct observation of sequential dissociation events of the polyatomic molecule could be plausible with the velocity map ion imaging technique.

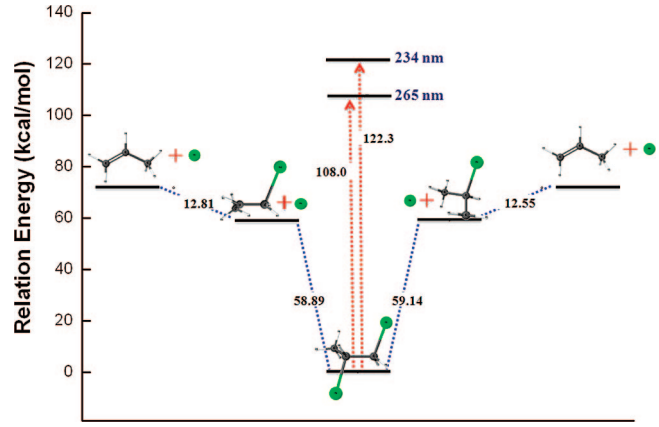

Figure 5. Energetics and optimized geometries of 1,2-dibromopropane, 1-bromopropyl radical, 2-bromopropyl radical, and propene obtained by the DFT calculation with the B3LYP method by using the 6-311++G(3df,3pd) basis set. Possible transition states or intermediates along the reaction paths are not considered in the calculation.

Acknowledgment. S.K.K. wishes Steve's continuing great scientific achievements for many more years to come. This work was supported by Eco-technopia 21 project of KIEST (102-071-606), KISTI supercomputing center (KSC-2007-S00-2010), KOSEF (R01-2007-000-10766-0, M10703000936-07M0300-93610), and the Center for Space-Time Molecular Dynamics (R11-2007-012-01002-0).

References and Notes

(1) Mulliken, R. S. *J. Chem. Phys.* **1940**, *8*, 382.
(2) Riley, S. J.; Wilson, K. R. *Faraday Discuss. Chem. Soc.* **1972**, *53*, 132.
(3) Gendanken, A.; Rowe, M. D. *Chem. Phys. Lett.* **1975**, *34*, 39.
(4) Shapiro, M.; Bersohn, R. *J. Chem. Phys.* **1980**, *73*, 3810.
(5) Hermann, H. W.; Leone, S. R. *J. Chem. Phys.* **1982**, *76*, 4766.
(6) Brewer, P.; Das, P.; Ondrey, G.; Bersohn, R. *J. Chem. Phys.* **1983**, *79*, 720.
(7) Veen, G. N. A. V.; Baller, T.; Vries, A. E. D. *Chem. Phys.* **1985**, *92*, 59.
(8) Butler, L. J.; Hintsa, E. J.; Shane, S. F.; Lee, Y. T. *J. Chem. Phys.* **1987**, *86*, 2051.
(9) Penn, S. M.; Hayden, C. C.; Muyskens, K. J. C.; Crim, F. F. *J. Chem. Phys.* **1988**, *89*, 2909.
(10) Loo, R. O.; Haerri, H.-P.; Hall, G. E.; Houston, P. L. *J. Chem. Phys.* **1989**, *90*, 4222.
(11) Lao, K. Q.; Person, M. D.; Xayariboun, P.; Butler, L. J. *J. Chem. Phys.* **1990**, *92*, 823.
(12) Chandler, D. W.; Janssen, M. H. M.; Stolte, S.; Strickl, R. N., Jr.; Parker, D. H. *J. Phys. Chem.* **1990**, *94*, 4839.

(13) Fairbrother, D. H.; Briggman, K. A.; Weitz, E.; Stair, P. C. *J. Chem. Phys.* **1994**, *101*, 3787.
(14) Thelen, M.-A.; Felder, P. *Chem. Phys.* **1996**, *204*, 135.
(15) Butler, L. J.; Neumark, D. M. *J. Phys. Chem.* **1996**, *100*, 12801.
(16) Gougousi, T.; Samartzis, P. C.; Kitsopoulos, T. N. *J. Chem. Phys.* **1998**, *108*, 5742.
(17) Jung, Y. J.; Park, M. S.; Kim, Y. S.; Jung, K. H.; Volpp, H.-R. *J. Chem. Phys.* **1999**, *111*, 4005.
(18) McGivern, W. S.; Li, R.; Zou, P.; North, S. W. *J. Chem. Phys.* **1999**, *111*, 5771.
(19) Zou, P.; McGivern, W. S.; North, S. W. *Phys. Chem. Chem. Phys.* **2000**, *2*, 3785.
(20) McGivern, W. S.; Sorkhabi, O.; Suits, A. G.; Derecskei-Kovacs, A.; North, S. W. *J. Phys. Chem. A* **2000**, *104*, 10085.
(21) Kavita, K.; Das, P. K. *Chem. Phys. Lett.* **2001**, *338*, 118.
(22) Kim, T. K.; Lee, K. W.; Lee, E. K.; Jung, K. H. *Chem. Phys. Lett.* **2007**, *446*, 31.
(23) Lipciuc, M. L.; Janssen, M. H. M. *J. Chem. Phys.* **2007**, *127*, 224310.
(24) Underwood, J. G.; Powis, I. *Phys. Chem. Chem. Phys.* **2000**, *1*, 747.
(25) Park, M. S.; Lee, K. W.; Jung, K.-H. *J. Chem. Phys.* **2001**, *114*, 10368.
(26) Park, M. S.; Kim, T. K.; Lee, S.-H.; Jung, K.-H.; Volpp, H.-R.; Wolfrum, J. *J. Phys. Chem. A* **2001**, *105*, 5606.
(27) Lee, Y. R.; Chou, C. C.; Lee, Y. J.; Wang, L. D.; Lin, S. M. *J. Chem. Phys.* **2001**, *115*, 3195.
(28) Lee, Y. R.; Chen, C. C.; Lin, S. M. *J. Chem. Phys.* **2003**, *118*, 10494.
(29) Tang, Y.; Ji, L.; Zhu, R.; Wei, Z.; Zhang, B. *J. Phys. Chem. A* **2005**, *109*, 11123.
(30) Fan, H.; Pratt, S. T.; Miller, J. A. *J. Chem. Phys.* **2007**, *127*, 144301.
(31) Kim, S. K.; Pedersen, S.; Zewail, A. H. *J. Chem. Phys.* **1995**, *103*, 477.
(32) Ueyama, M.; Hasegawa, H.; Hishikawa, A.; Yamanouchi, K. *J. Chem. Phys.* **2005**, *123*, 154305.
(33) Nalda, R.; Izquierdo, J. G.; Durá, J.; Bañares, L. *J. Chem. Phys.* **2007**, *126*, 021101.
(34) Lee, K.-S.; Lee, K. W.; Kim, T. K.; Ryoo, R.; Jung, K.-H. *J. Chem. Phys.* **2005**, *122*, 034308.
(35) Eppink, A. T. J. B.; Parker, D. H. *Rev. Sci. Instrum.* **1997**, *68*, 3477.
(36) Eppink, A. T. J. B.; Parker, D. H. *J. Chem. Phys.* **1998**, *109*, 4758.
(37) Whitaker, B. J. *Imaging in Molecular Dynamics: Technology and Applications*; Cambridge University Press: Cambridge, 2003.
(38) Lee, K.-S.; Lim, J. S.; Ahn, D. S.; Choi, K. W.; Kim, S. K.; Choi, Y. S. *J. Chem. Phys.* **2006**, *124*, 124307.
(39) Frisch, M. J.; Trucks, G. W.; Schlegel, H. B.; Scuseria, G. E.; Robb, M. A.; Cheeseman, J. R.; Montgomery, J. A., Jr.; Vreven, T.; Kudin, K. N.; Burant, J. C.; Millam, J. M.; Iyengar, S. S.; Tomasi, J.; Barone, V.; Mennucci, B.; Cossi, M.; Scalmani, G.; Rega, N.; Petersson, G. A.; Nakatsuji, H.; Hada, M.; Ehara, M.; Toyota, K.; Fukuda, R.; Hasegawa, J.; Ishida, M.; Nakajima, T.; Honda, Y.; Kitao, O.; Nakai, H.; Klene, M.; Li, X.; Knox, J. E.; Hratchian, H. P.; Cross, J. B.; Bakken, V.; Adamo, C.; Jaramillo, J.; Gomperts, R.; Stratmann, R. E.; Yazyev, O.; Austin, A. J.; Cammi, R.; Pomelli, C.; Ochterski, J. W.; Ayala, P. Y.; Morokuma, K.; Voth, G. A.; Salvador, P.; Dannenberg, J. J.; Zakrzewski, V. G.; Dapprich, S.; Daniels, A. D.; Strain, M. C.; Farkas, O.; Malick, D. K.; Rabuck, A. D.; Raghavachari, K.; Foresman, J. B.; Ortiz, J. V.; Cui, Q.; Baboul, A. G.; Clifford, S.; Cioslowski, J.; Stefanov, B. B.; Liu, G.; Liashenko, A.; Piskorz, P.; Komaromi, I.; Martin, R. L.; Fox, D. J.; Keith, T.; Al-Laham, M. A.; Peng, C. Y.; Nanayakkara, A.; Challacombe, M.; Gill, P. M. W.; Johnson, B.; Chen, W.; Wong, M. W.; Gonzalez, C.; Pople, J. A. *Gaussian 03*, revision D.01; Gaussian, Inc.: Wallingford, CT, 2004.
(40) Dribinski, V.; Ossadtchi, A.; Mandelshtam, V. A.; Reisler, H. *Rev. Sci. Instrum.* **2002**, *73*, 2634.

JP8022666